



click for updates

## Polymorphism driven optical properties of an anil dye†

Cite this: DOI: 10.1039/c6ce00266h

Damir A. Safin,<sup>a</sup> Koen Robeyns,<sup>a</sup> Maria G. Babashkina,<sup>a</sup> Yaroslav Filinchuk,<sup>a</sup> Aurelian Rotaru,<sup>b</sup> Catalin Jureschi,<sup>b</sup> Mariusz P. Mitoraj,<sup>\*c</sup> James Hooper,<sup>c</sup> Mateusz Breła<sup>c</sup> and Yann Garcia<sup>\*a</sup>

Red crystals of *N,N'*-bis(3-methoxysalicylidene)-1,5-diiminonaphthalene were obtained after Schiff base condensation in ethanol. Recrystallization from acetone afforded yellow crystals, a process which is reversible and reproducible. Single crystal X-ray diffraction evidences two polymorphs differing in their space group and dihedral angle between aromatic moieties. DFT periodic calculations further confirmed the existence of two minima on the potential energy surface corresponding to red and yellow crystals. The red polymorph irreversibly (monotropically) transforms at 165–190 °C into the yellow one with a 3% increase of the unit cell volume, as shown by X-ray powder diffraction and periodic DFT calculations. Both polymorphs are thermochromic but only the red one displays photochromism upon irradiation at  $\lambda = 365$  nm, which is reversible and exhibits a relatively slow thermal relaxation. A temperature induced *cis/trans*-keto equilibrium is for the first time identified for an *N*-salicylidene aniline derivative. Static DFT molecular and periodic calculations as well as *ab initio* Born–Oppenheimer dynamics simulations were performed to characterize the stability of both polymorphs and to determine the relative populations of the enol/*cis*-keto/*trans*-keto isomers at various temperatures.

Received 1st February 2016,  
Accepted 1st March 2016

DOI: 10.1039/c6ce00266h

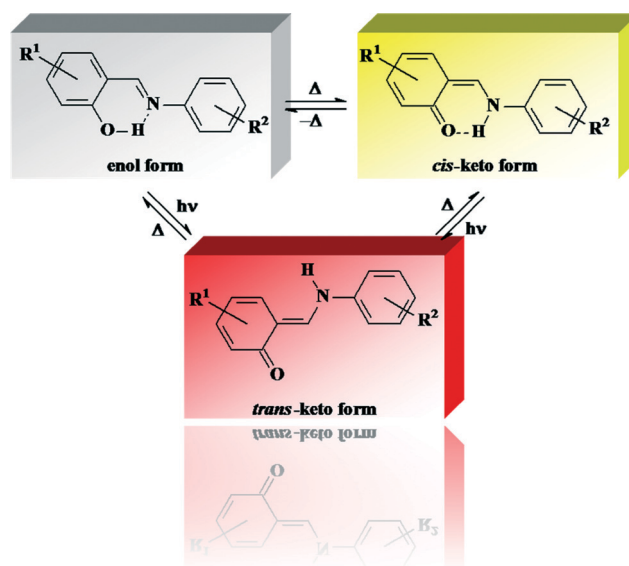
www.rsc.org/crystengcomm

## Introduction

Nowadays optical devices are playing a considerable role in both daily life and instrumentation.<sup>1</sup> Molecular switches displaying reversible solid state thermo- and photochromism phenomena are considered as outstanding candidates for implementation into smart devices.<sup>2</sup> Among the rare classes of photochromic molecules operating in the crystalline state,<sup>3</sup> *N*-salicylidene aniline derivatives play a dominant role due to their colour panel and accessible forms (Scheme 1).<sup>4</sup> In addition, the possibility of being included into various matrices to form hybrid materials,<sup>5</sup> blends,<sup>6</sup> and even coordination complexes,<sup>7</sup> increases their attractiveness from a synthetic point of view.

Primarily, the solid state thermochromism of *N*-salicylidene aniline derivatives is considered to result from

the planarity of the molecule and the formation of a “close-packed crystal structure” (dihedral angle between the aromatic rings  $\Phi < 25^\circ$ ), whereas photochromism is caused by the significant rotation of aromatic rings and the formation of an “open structure” ( $\Phi > 25^\circ$ ).<sup>3b,4d</sup> Thermo- and photochromic properties were claimed over the years to be mutually



Scheme 1

<sup>a</sup> Institute of Condensed Matter and Nanosciences, Molecules, Solids and Reactivity (IMCN/MOST), Université catholique de Louvain, Place L. Pasteur 1, 1348 Louvain-la-Neuve, Belgium. E-mail: damir.a.safin@gmail.com, yann.garcia@uclouvain.be; Fax: +32 1047 2330; Tel: +32 1047 2831

<sup>b</sup> Faculty of Electrical Engineering and Computer Science, and Research Center MANSiD, Stefan cel Mare University, Str. Universitatii, No. 13, 720229 Suceava, Romania

<sup>c</sup> Department of Theoretical Chemistry, Faculty of Chemistry, Jagiellonian University, R. Ingardena 3, 30-060 Cracow, Poland.

E-mail: mitoraj@chemia.uj.edu.pl

† Electronic supplementary information (ESI) available: Additional data, Fig. S1–S16 and Tables S1–S4. CCDC 881637 and 881638. For ESI and crystallographic data in CIF or other electronic format see DOI: 10.1039/c6ce00266h

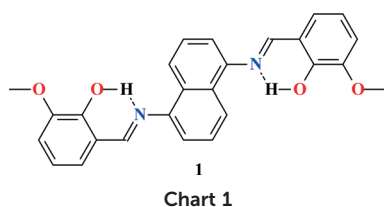
exclusive.<sup>4b</sup> A number of contradicting examples showing both thermo- and photochromic properties have been however recently discussed.<sup>7a,8,9</sup> Hence, it is currently not possible to explain the thermo- and photochromism of *N*-salicylidene aniline derivatives on the sole basis of their crystal structures. Energy differences between ground and excited states need also to be considered,<sup>7a</sup> as well as a complete crystal structure determination including crystal packing,  $\Phi$  and the available free space around the switching unit in addition to the flexibility of the nearby environment.<sup>9</sup>

The thermo- and photochromic properties of mono-*N*-salicylidene aniline derivatives have been thoroughly studied,<sup>4,7a,8</sup> but bis(salicylidene)<sup>8d,10</sup> and tris(salicylidene)<sup>11</sup> derivatives have attracted much less attention from an optical properties point of view. Herein, we report the synthesis, crystal structure and optical properties of red and yellow solvent-free polymorphs of *N,N'*-bis(3-methoxysalicylidene)-1,5-diiminonaphthalene (**1**) (Chart 1). Furthermore, the solvent-induced interconversion and temperature-induced phase transitions of both polymorphs were studied. We also provide a detailed description of the previously reported yellow polymorph<sup>12</sup> for a better and in-depth comparison with the red polymorph.

## Results and discussion

The bis-anil **1** was synthesized by reacting 1,5-diaminonaphthalene with *o*-vanilin in ethanol. The as-synthesized compound forms red crystals (**1red**), which are soluble in most polar solvents and water and are insoluble in *n*-hexane and diethylether. Recrystallization of **1red** from acetone gives yellow crystals (**1yellow**). Recrystallization of **1yellow** from ethanol or methanol gives back crystals of **1red**. Thus, this solvent-induced interconversion is reversible and reproducible.

<sup>1</sup>H NMR spectra of **1** both in CDCl<sub>3</sub> and DMSO-*d*<sub>6</sub> are very similar. The spectra reveal a single set of signals, which testifies to a symmetric structure of **1** in both solvents. The signal for the CH<sub>3</sub> protons was found at 3.87–3.99 ppm, while a number of doublet and triplet signals for the benzene and naphthalene protons were observed at 6.97–8.28 ppm. The signals of the CNH and OH protons in the spectra of **1** were shown at 8.78–9.06 and 13.09–13.88 ppm. <sup>1</sup>H NMR spectra of both polymorphs are the same regardless of the solvent. Minor differences are exclusively due to different polarities of these solvents.



**1red** and **1yellow** crystallize in the monoclinic space groups  $P2_1/c$  and  $P2_1/n$ , respectively. Each molecule was found in the enolimine form. The bond lengths of O(16)–C(13) are about 1.35 Å and those of C(8)–C(7) are about 1.45 Å, which indicates single bonds, whereas a double bond of about 1.28 Å is revealed for N(6)–C(7) (Table S1 in the ESI†). The bond angles C(4)–N(6)–C(7) of 121.02(13)–121.24(19)° indicate the sp<sup>2</sup>-hybridization of nitrogen atoms, further supporting the enolimine form (Table S1 in the ESI†). The crucial difference between the structures of the two polymorphs consists of the dihedral angle  $\Phi$  between benzene and naphthalene rings (Fig. 1). In **1red** the two rings are at 21.34(10)°, while the dihedral angle is significantly larger in **1yellow**, reaching 47.13(7)° (Fig. 1, Table S1 in the ESI†). The crystal structures of both polymorphs are stabilized by two intramolecular hydrogen bonds O(16)–H(16)⋯N(6) (Table S2 in the ESI†).

The bulk samples of both **1red** and **1yellow** were studied by means of X-ray powder diffraction analysis. The experimental X-ray powder patterns are in agreement with the calculated powder patterns obtained from the single crystal X-ray analyses, showing that the bulk materials **1red** and **1yellow** are free from phase impurities.

In order to examine the interactions in the crystal structures of both polymorphs, the Hirshfeld surface analysis<sup>13</sup> and associated 2D fingerprint plots<sup>14</sup> were obtained using CrystalExplorer 3.1.<sup>15</sup>

According to the Hirshfeld surface analysis, for **1red** the intermolecular H⋯H contacts, comprising 45.9% of the total number of contacts, are major contributors to the crystal packing, while the same contacts for **1yellow** are significantly lower (37.6%) (Table S3 in the ESI†). The shortest H⋯H contacts are shown in the fingerprint plot of **1red** as characteristic spikes at  $d_e + d_i \approx 2.1$  Å (Fig. 2). The shortest H⋯H contacts in the fingerprint plot of **1yellow** are however observed at  $d_e + d_i \approx 2.5$  Å (Fig. 2). Furthermore, a subtle feature is evident in the fingerprint plot of **1red**. There is a splitting of the short H⋯H fingerprint. This splitting occurs when the shortest contact is between three atoms, rather than for a direct two-atom contact.<sup>15</sup>

The structure of **1red** is also dominated by H⋯C contacts, comprising 24.1%, while the same contacts in the structure of **1yellow** are the most abundant and occupy 39.2% of the total Hirshfeld surface areas (Table S3 in the ESI†). These

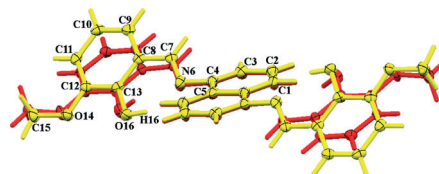


Fig. 1 Overlaid molecules in **1red** and **1yellow** (50% atomic displacement ellipsoids are shown). The dihedral angles formed by the benzene and naphthalene rings are different in the two forms (21.3° vs. 47.1°).

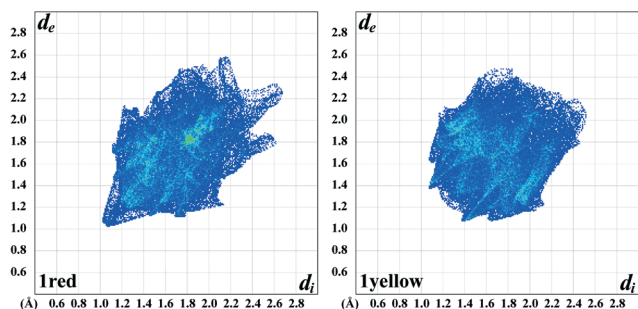


Fig. 2 2D fingerprint plots of observed contacts for both polymorphs.

contacts in fingerprint plots are shown in the form of clearly pronounced “wings” (Fig. 2), with the shortest  $d_e + d_i \approx 2.6$ – $2.8$  Å. These contacts are recognized as characteristic of the C–H $\cdots$  $\pi$  nature.<sup>15</sup> It is worth adding that the fingerprint plot of **1red** exhibits a significant number of points at large  $d_e$  and  $d_i$ , shown as tails at the top right of the plot (Fig. 2). These points, similar to those observed in the fingerprint plots of benzene<sup>15</sup> and phenyl-containing compounds,<sup>16</sup> correspond to regions on the Hirshfeld surface without any close contacts to nuclei in adjacent molecules.

The third main contribution into intermolecular interactions in the structures of **1red** and **1yellow** arises from H $\cdots$ O contacts, comprising 16.6% and 18.1% of the total Hirshfeld surface areas, respectively (Table S3 in the ESI<sup>†</sup>). The structures of both polymorphs are also described by C $\cdots$ C contacts. However, these contacts comprise a negligible proportion of the total Hirshfeld surface area in the structure of **1yellow** and of 1.7%, while they occupy 6.7% of the surface in the structure of **1red** (Table S3 in the ESI<sup>†</sup>). Moreover, these contacts are shown on the fingerprint plot of **1red** as the area of pale blue colour on the diagonal at  $d_e = d_i \approx 1.8$ – $1.9$  Å (Fig. 2). These contacts are evidence for  $\pi\cdots\pi$  stacking interactions in the crystal structure of **1red**.

Close inspection of other intermolecular contacts in the structure of **1red** also revealed a proportion of C $\cdots$ N (5.0%) and C $\cdots$ O (1.7%) contacts (Table S3 in the ESI<sup>†</sup>). A negligible amount (0.6%) of the latter contacts as well as H $\cdots$ N (2.8%) contacts was also found in the structure of **1yellow**.

We have also determined the enrichment ratios ( $E$ )<sup>17</sup> of the intermolecular contacts for both polymorphs to study the propensity of two chemical species to be in contact. The enrichment ratio, derived from the Hirshfeld surface analysis, is defined as the ratio between the proportion of actual contacts in the crystal and the theoretical proportion of random contacts.  $E$  is larger than unity for pairs of elements with a higher propensity to form contacts, while pairs which tend to avoid contacts yield an  $E$  value lower than unity.

The H $\cdots$ H contacts are favoured in the structure of **1red** since the enrichment ratio  $E_{\text{HH}}$  is close to unity (1.05) and generate a majority (45.9%) of the interaction surface (Table S3 in the ESI<sup>†</sup>). Contrarily, the H $\cdots$ H contacts are only slightly favoured in the structure of **1yellow** ( $E_{\text{HH}} = 0.82$ ). This is explained by a significantly lower proportion (37.6%) of

H $\cdots$ H contacts of the total Hirshfeld surface area in **1yellow**, although its structure contains almost the same amount of random contacts as in the structure of **1red** (Table S3 in the ESI<sup>†</sup>). The *vice versa* trend is observed for H $\cdots$ C contacts, which show an increased propensity to form ( $E_{\text{HC}} = 1.34$ ) in the structure of **1yellow**, and only slightly favoured ( $E_{\text{HC}} = 0.82$ ) in **1red**. This is due to a significantly higher amount of H $\cdots$ C contacts of the total Hirshfeld surface area in **1yellow** compared to that in **1red**, despite both structures being characterised by the same values of the  $S_{\text{H}}$  proportion and random contacts  $R_{\text{HC}}$  (Table S3 in the ESI<sup>†</sup>). The  $E_{\text{HO}}$  values are larger than unity ( $\sim 1.40$ ) for both polymorphs, indicating that H $\cdots$ O contacts have an increased propensity to form with close random contacts ( $\sim 12.5\%$ ). It should be noted that H $\cdots$ N contacts are highly favoured in the structure of **1yellow** since the enrichment ratio  $E_{\text{HN}}$  is remarkably higher than unity (1.47), while the same contacts in the structure of **1red** are completely absent. The structure of **1red** is further characterized by significantly impoverished C $\cdots$ O contacts ( $E_{\text{CO}} = 0.43$ ), while the same contacts in the structure of **1yellow** are even much more impoverished ( $E_{\text{CO}} = 0.15$ ). Interestingly, the C $\cdots$ C contacts in the structure of **1red** are remarkably enriched ( $E_{\text{CC}} = 1.37$ ), which is due to a relatively high value of their proportion of the total Hirshfeld surface area. Although the  $S_{\text{C}}$  value and random contacts proportion  $R_{\text{CC}}$  of the structure of **1yellow** are almost the same as those for **1red**, its structure is characterized by very impoverished C $\cdots$ C contacts ( $E_{\text{CC}} = 0.36$ ). This is explained by a negligible amount of C $\cdots$ C contacts on the molecular surface of **1yellow** (Table S3 in the ESI<sup>†</sup>).

The thermal stability of **1red** and **1yellow** was studied by means of simultaneous TG/DSC. The thermal decomposition process is very similar for both polymorphs (Fig. S1 in the ESI<sup>†</sup>). First, one endothermic effect was identified at 220 °C for **1yellow**, corresponding to its melting point, while two very close exothermic anomalies at 219 °C and 223 °C were observed for **1red**. Two exothermic peaks were identified on warming further at 356 °C and 547 °C, both for **1red** and **1yellow**. The first is associated to the formation of elemental carbon, which is burnt after the second decomposition step leading to carbon dioxide. Differential scanning calorimetry (DSC) runs of **1red** and **1yellow** were recorded from 100 to 250 °C on both warming and cooling (Fig. S2 and S3 in the ESI<sup>†</sup>). The yellow polymorph exhibits one endo- and two exothermic peaks, corresponding to the melting and crystallization processes, respectively, regardless of the run number (Fig. S3 in the ESI<sup>†</sup>). The red polymorph exhibits two anomalies upon warming and only one on cooling for the first run, while only one peak was fixed upon warming and cooling during the second run (Fig. S2 in the ESI<sup>†</sup>). These DSC observations for **1red** might be explained by the presence of a mixture of both polymorphs during warming of **1red**, which exhibits an irreversible (monotropical) phase transition at 165–190 °C from the red polymorph to the yellow one. Interestingly, the double thermal anomaly transformed to one for **1red** after warming for a second run (Fig. S2 in the ESI<sup>†</sup>).

Single crystals of **1yellow** display weak thermochromism to pale yellow on cooling to  $-190\text{ }^{\circ}\text{C}$  (Fig. 3), as expected with the major formation of the enol form. On warming **1yellow** turns red at  $200\text{ }^{\circ}\text{C}$ , due to the formation and further population of the *trans*-keto form within the same **1yellow** polymorph. Single crystals of **1red** also reveal thermochromism to pale yellow on cooling to  $-190\text{ }^{\circ}\text{C}$ , but turn dark red on warming to  $200\text{ }^{\circ}\text{C}$  (Fig. 3). This observation stems from the **1red** to **1yellow** transition, evidenced by X-ray diffraction (see X-ray powder diffraction studies below), followed by the population of the *trans*-keto form within the same **1yellow** polymorph. A different crystal quality is also detected by optical microscopy with a large number of crystal twinnings for **1red** compared to **1yellow**. Atomic force microscopy (AFM) images also show different morphologies with the surface of **1yellow** which reveals a wave-like shape (Fig. S4 in the ESI<sup>†</sup>), whereas a slice-like shape is found for **1red** (Fig. S5 in the ESI<sup>†</sup>). The surface roughness was evaluated to be  $\sim 300\text{ nm}$  for both polymorphs.

Polymorphs **1red** and **1yellow** were also analyzed by diffuse reflectance spectroscopy (DRS) as pure solid powders to avoid matrix and environment effects that are known to intensively modify the optical properties of *N*-salicylidene aniline derivatives.<sup>18</sup> Diffuse reflectance spectra, for which a Kubelka–Munk (KM) treatment was applied, exhibit two main band regions: a broad band range in the UV region, corresponding to the enol form, and a second range in the visible region from about 385 to 480 nm, originating from the *cis*-keto form. A third range above 475 nm, originating from the *trans*-keto form, is delineated (Fig. 4). A major contribution is found for **1red** whereas only traces of *trans*-keto form are detected for **1yellow** (Fig. 3). **1red** and **1yellow** were also analyzed by DRS upon irradiation at selected wavelengths ( $\lambda = 254, 365, 450$  and  $546\text{ nm}$ ) in order to photo-address enol and keto forms.

Contrary to expectations based on dihedral angle  $\Phi$  considerations, **1red** is photochromic upon irradiation at  $\lambda = 365\text{ nm}$  (Fig. 5), although it was expected to be only thermochromic ( $\Phi < 25^{\circ}$ ), and **1yellow** is only thermochromic, whereas it was expected to be also photochromic ( $\Phi > 25^{\circ}$ ).<sup>3b,4d</sup>

We have examined the reversibility of the *cis*-keto/*trans*-keto isomerization for **1red** (Fig. 6). Irradiation of **1red** at

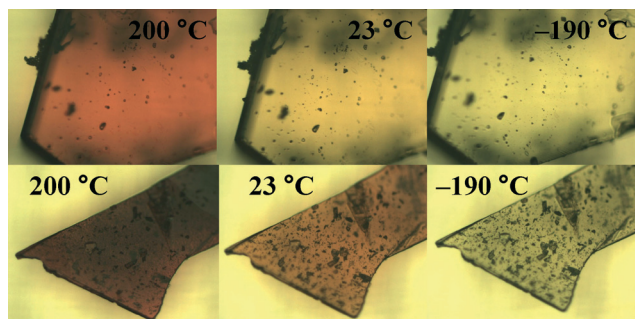


Fig. 3 Optical images showing thermochromism for single crystals of **1yellow** (top) and **1red** (bottom).

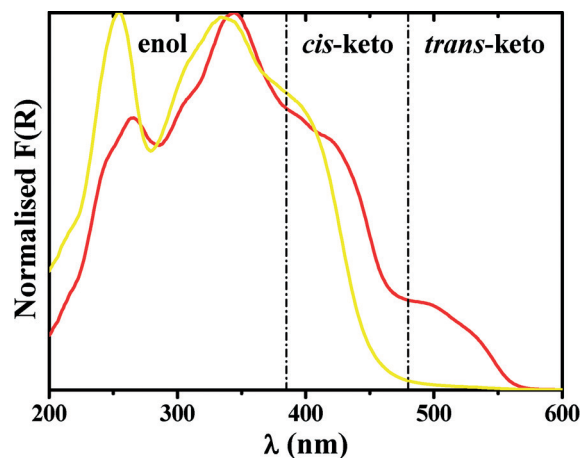


Fig. 4 Normalized KM spectra of **1red** (red) and **1yellow** (yellow) at  $23\text{ }^{\circ}\text{C}$ .

$\lambda_{\text{max}} = 365\text{ nm}$  for 30 min results in an increase of the KM function  $F(R)$ . Thermal relaxation to the *trans*-keto form is rather slow and the data are fitted best using a first-order exponential equation. The kinetic constant of **1red** ( $k = 6.0 \times 10^{-5}\text{ s}^{-1}$ ) is rather low and attributed to a weak decreasing photochromism. A similar slow back thermal relaxation was observed for  $(2\text{-OH-(5-Br)C}_6\text{H}_3\text{C=N})_2\text{-}m\text{-C}_6\text{H}_4$  ( $k = 2.6 \times 10^{-5}\text{ s}^{-1}$ )<sup>19</sup> and  $2,4\text{-(OH)}_2\text{C}_6\text{H}_3\text{CH=N-(4-COOMe)C}_6\text{H}_4$  ( $k = 2.7 \times 10^{-5}\text{ s}^{-1}$ ).<sup>20</sup> The lowest kinetic constants were found for  $2\text{-OH-3,5-}t\text{Bu}_2\text{C}_6\text{H}_2\text{CH=N-3-C}_6\text{H}_4$  ( $k = 2.0 \times 10^{-7}\text{ s}^{-1}$ ),<sup>21</sup>  $2\text{-OH-C}_6\text{H}_4\text{CH=N-3-Py}$  ( $k = 9.9 \times 10^{-8}\text{ s}^{-1}$ )<sup>7a</sup> and  $2\text{-OH-3,5-}t\text{Bu}_2\text{C}_6\text{H}_2\text{CH=N-4-Py}$  ( $k = 1.8 \times 10^{-8}\text{ s}^{-1}$ ).<sup>20</sup> The elaborated thermal relaxation, containing more than one chemical relaxation pathway, was recently found for *N,N'*-bis(salicylidene)-*m*-phenylenediamine,<sup>11b,22</sup> *N*-salicylidene 4-amino-3,5-bis(pyridine-2-yl)-1,2,4-triazole<sup>8a</sup> and 5-chloro-*N*-salicylidene-3-aminomethylpyridine.<sup>8b</sup>

The reversibility of the *cis*-keto/*trans*-keto isomerization of **1red** was studied. After photoexcitation at  $\lambda = 365\text{ nm}$  and thermal relaxation over 10 h, irradiation at  $\lambda = 546\text{ nm}$

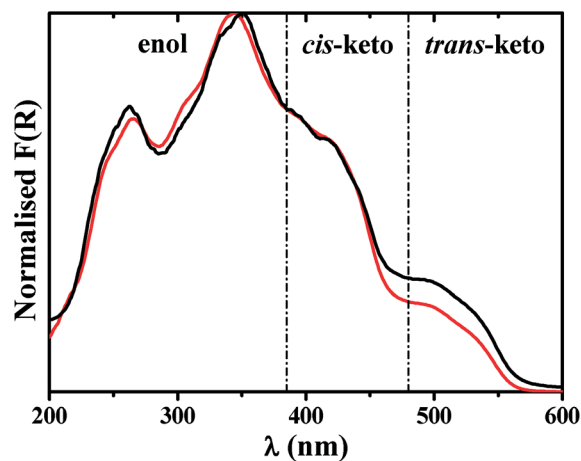


Fig. 5 Normalized KM spectra of **1red** before (red) and after (black) irradiation at  $\lambda = 365\text{ nm}$  for 30 min at  $23\text{ }^{\circ}\text{C}$ .

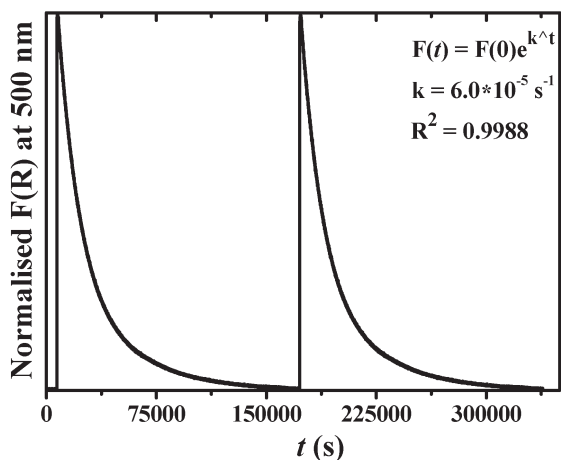


Fig. 6 Normalized time dependence of the KM function  $F(R)$  of **1red** at 500 nm showing a thermal relaxation of the metastable *trans*-keto form with cycles of irradiation at  $\lambda = 365$  nm.

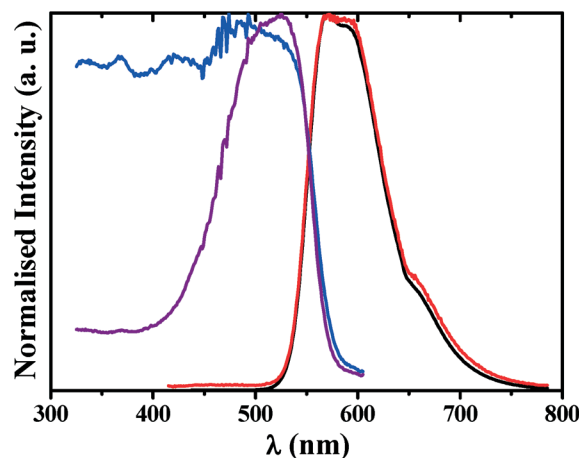


Fig. 8 Normalized solid-state emission and excitation spectra of **1red** (Em – black, Ex – blue) and **1yellow** (Em – red, Ex – purple) at 23 °C ( $\lambda^{\text{exc}} = 400$  nm,  $\lambda^{\text{em}} = 620$  nm).

induces a fast return to the initial  $F(R)$  value. The cycle can be repeated by irradiation once again at  $\lambda = 365$  nm (Fig. 7).

Solid state fluorimetric studies of **1red** and **1yellow** crystals were undertaken to examine the energy levels responsible for the photoswitchable optical properties. The emission spectra of both polymorphs at  $\lambda^{\text{exc}} = 400$  nm, which corresponds to the absorption band of the *cis*-keto form (Fig. 4), are very similar (Fig. 8). Two intense bands centered at 570 and 593 nm are observed for **1red** and **1yellow**. The fluorescence has been assigned to the emission from the *cis*-keto form, which is produced through the proton transfer in the excited state of the enol form. Therefore, an anomalously large Stokes shift is observed. The longer wavelength band originates from the emission of the more stable and relaxed conformation of the *cis*-keto form and the band at the shorter wavelength is due to the emission from the less stable planar conformation.<sup>23</sup> A third weak emission band is also noted at about 650 nm for both polymorphs in the region of the

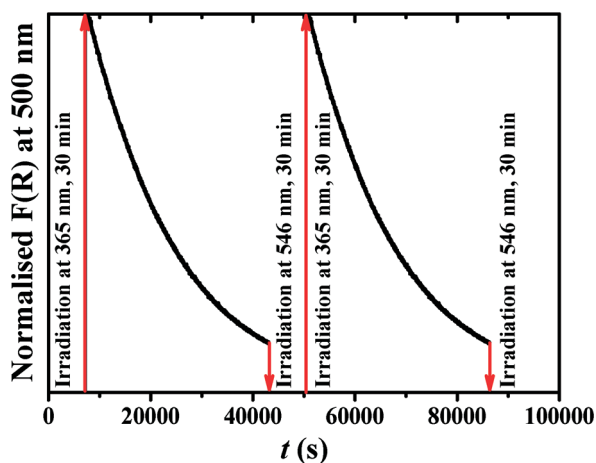


Fig. 7 Reversibility of the *cis/trans*-keto isomerization of **1red** as shown by the evolution of the normalized KM function  $F(R)$  at 500 nm with cycles of irradiation at  $\lambda = 365$  and  $\lambda = 546$  nm.

*trans*-keto form, as deduced from diffuse reflectance data (Fig. 4).

Excitation spectra of **1red** and **1yellow** recorded at  $\lambda^{\text{em}} = 620$  nm reveal a main contribution from the band centred at about 525 nm, which is noted for **1red** and more surprisingly for **1yellow** (Fig. 8). This band can be assigned to the absorption of the *trans*-keto form by comparison with diffuse reflectance spectroscopy (Fig. 4). The emission at about 650 nm can thus be assigned to the radiative relaxation of the *trans*-keto\* form, which can be formed through the absorption of enol, *cis*-keto and *trans*-keto forms in their ground state.<sup>8b,c,20</sup>

Temperature evolution of **1red** and **1yellow** was studied by X-ray powder diffraction in order to study the possible thermal interconversion between both polymorphs. No phase transition was observed from about liquid nitrogen temperature and up to the melting of **1yellow**, while **1red** shows no changes on cooling from room temperature down to about liquid nitrogen temperature. Furthermore, **1red** exhibits on heating an irreversible (monotropical) phase transition to **1yellow** (Fig. 9). At 27 °C h<sup>-1</sup> heating rate a dramatic increase of the unit cell volume by ~3% was noticed above 165 °C. Melting of the yellow phase is observed above 220 °C (Fig. S6 in the ESI†) in agreement with the DSC data (Fig. S2 in the ESI†). Moreover, the volumetric thermal expansion coefficient of **1yellow** ( $2.09(4) \times 10^{-4}$ ) is significantly larger than that for **1red** ( $1.28(1) \times 10^{-4}$ ). The thermal expansion is almost linear for both phases.

These results have been confirmed by variable temperature optical reflectivity measurements on polycrystalline materials for both polymorphs, using a home-made setup. This technique has been widely applied to follow the colour change of thermochromic materials, in particular spin state switchable materials.<sup>24</sup>

Reflectance data of **1red** decreases slowly over the temperature range from -190 °C to 0 °C (Fig. 10), in agreement with the weak colour change expected on warming from the enol

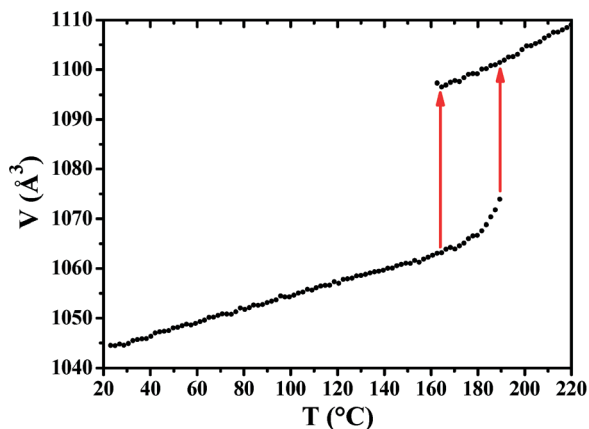


Fig. 9 Evolution of the unit cell volume upon heating **1red**, as observed by X-ray powder diffraction. The irreversible (monotropical) phase transition to **1yellow** occurs at  $\sim 165$ – $190$  °C. The transition is accompanied by a 3% volume increase, along with the 63% increase of the volumetric thermal expansion coefficient.

to *cis*-keto forms population as already noted in Fig. 3. Reflectance further decreases on warming to plateau around 165 °C, after which a dramatic jump is observed. This latter behaviour, which indicates a darkening of the colour, in full agreement with Fig. 3, corresponds to the irreversible (monotropical) phase transition of **1red** to **1yellow** which was already observed by X-ray powder diffraction (Fig. 9), and followed by *trans*-keto form population within the same **1yellow** polymorph (Fig. 3). On cooling and warming again, no dramatic change is observed. A similar behaviour in the thermal dependence of the reflectance data has been observed on **1yellow**, except that the slope on warming over the temperature range from  $-190$  °C to  $0$  °C (Fig. 10) is weaker compared to **1red**, in agreement with Fig. 3, which reveals less colour change on cooling. On warming further above 150 °C, a dramatic decrease is observed, in agreement with the *trans*-keto form population of the **1yellow** polymorph. The next cooling and warming run did not lead to any colour change.

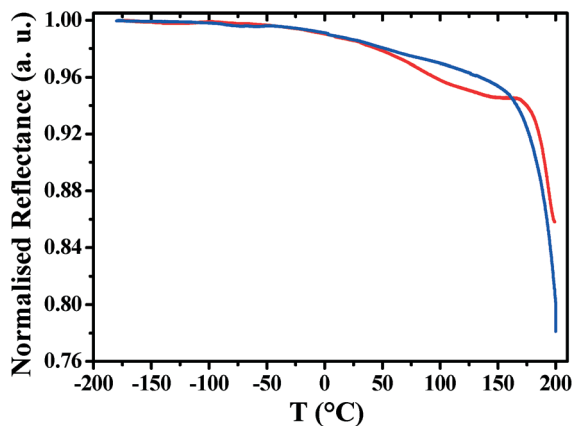


Fig. 10 Thermal dependence of the normalized reflectance recorded on a polycrystalline sample of **1red** (red) and **1yellow** (blue).

In order to shed additional light on the enol/*cis*-keto/*trans*-keto equilibrium of **1**, we have performed static DFT molecular calculations based on the ADF program<sup>25</sup> with DFT/BLYP-D3/TZP. Subsequently, we have extended our modelling by carrying out static periodic DFT calculations applying the VASP program<sup>26</sup> as well as *ab initio* molecular dynamics simulations of crystals by means of the CP2K package.<sup>27</sup>

It was established that the enol/enol form of **1**, containing two intramolecular hydrogen bonds of the O–H $\cdots$ N type, is more stable than the *cis*-keto/*cis*-keto form, exhibiting two intramolecular hydrogen bonds of the N–H $\cdots$ O type, by  $\Delta G = 3.5$  kcal mol $^{-1}$  (Fig. 11). An intermediate enol/*cis*-keto geometry has an energy roughly halfway between enol/enol and *cis*-keto/*cis*-keto geometries. Thus, substitution of the O–H $\cdots$ N connections in enol by N–H $\cdots$ O ones leads to a subtle but systematic increase in free energy in the following order: enol/enol < enol/*cis*-keto < *cis*-keto/*cis*-keto. The *trans*-keto form, in which the benzoquinone groups are rotated such that both N–H $\cdots$ O contacts are broken, is the least stable isomer by about 26 kcal mol $^{-1}$  (Fig. 11). Clearly, the isolated molecule is stabilized by intramolecular hydrogen bonds in the enol and *cis*-keto forms. The small energy differences between the enol and *cis*-keto forms suggest that they can, as expected, be populated in the ground state at moderate temperatures. The calculated energy barrier for the enol to *cis*-keto transition is also quite small; it is computed to be  $\sim 7$  kcal mol $^{-1}$  at the DFT/BLYP-D3/TZP level of theory.

A comparison of how each O–H $\cdots$ N contact changes during the molecular dynamics (MD) simulations at 40, 300 and 500 K is shown in Fig. S7–S12 in the ESI $^\dagger$ . MD simulations on the crystal structure of **1yellow** confirm an equilibrium between the enol and *cis*-keto forms at room temperature (Fig. S11 and animation 1yellow-crystal-300K.wmv in the ESI $^\dagger$ ). The results of MD simulations on the crystal structure of **1red** (Fig. S8 and animation 1red-crystal-300K.wmv in the ESI $^\dagger$ ) are our first hint at intrinsic differences in the molecule–molecule interactions between **1yellow** and **1red**. In particular, **1red** clearly favours the *cis*-keto form over the enol form at room temperature with our DFT models. The higher

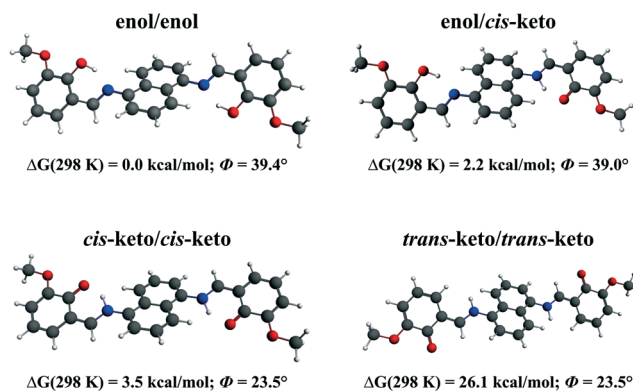


Fig. 11 The optimized structures together with relative free energies and dihedral angles  $\phi$  of different isomers of **1**, obtained from ADF/DFT/BLYP-D3/TZP calculations.

population of the *cis*-keto form within **1red** could be expected to result in a higher population of the geometrically related *trans*-keto isomer. This can explain why **1red** turns to a darker red at high temperature, while **1yellow** changes to a brighter and lighter shade of red (Fig. 3). At 40 K, all of the molecules remain trapped in their initial enol geometries, while a higher simulation temperature was found to increase the relative abundance of the *cis*-keto form in **1yellow** from 25% at 300 K to 35% at 500 K (Fig. 12). These results are consistent with the enol form of **1yellow** being more dominant at low temperature, and that is in agreement with the observation of thermochromism in both polymorphs to pale yellow at low temperature.

Rotation of a single phenyl ring in the *cis*-keto isomer, leading to a *trans*-keto geometry, costs about 40 kcal mol<sup>-1</sup> (Fig. S13 in the ESI†). It is likely that the barrier to such rotation in the crystal will be significantly lower due to intermolecular interactions. Therefore, it would be worth in the future to extend our model to a supercell containing more than one unit cell. This would shed more light on the *cis*-keto to *trans*-keto isomerization at various temperatures.

Static periodic DFT calculations, performed with the VASP computational package,<sup>26</sup> further demonstrate that **1yellow** favours the enol molecular conformer over the *cis*-keto form ( $\Delta E = -4.5$  kcal mol<sup>-1</sup>). This is again consistent with the experimental assertion that the enol form of **1yellow** becomes dominant at low temperature. However, the enol and *cis*-keto forms of **1red** are effectively thermoneutral with the latter form being slightly favoured by 0.4 kcal mol<sup>-1</sup>. This confirms that crystal packing effects, specifically those in **1red**, can overcome the inherent energetic preference of the enol molecular form, even at 0 K. The calculated values of dihedral

angles between the benzene and the naphthalene rings,  $\Phi = 42.6^\circ$  for **1yellow** and  $\Phi = 23.1^\circ$  for **1red**, fit quite well to the experimental data:  $\Phi = 47.1^\circ$  (**1yellow**) and  $\Phi = 21.3^\circ$  (**1red**).

The computed optimal volumes for our models of **1yellow** and **1red** are also in good agreement with the trends observed in the experimental results. The optimal volumes of **1yellow** were found to be  $V_{\text{enol}} = 1036 \text{ \AA}^3$  and  $V_{\text{cis-keto}} = 1032 \text{ \AA}^3$  ( $V_{\text{exp}} = 1036 \text{ \AA}^3$ ), and the optimal volumes of **1red** were found to be  $V_{\text{enol}} = 1028 \text{ \AA}^3$  and  $V_{\text{cis-keto}} = 1018 \text{ \AA}^3$  ( $V_{\text{exp}} = 1032 \text{ \AA}^3$ ).

The larger volume of **1yellow** is consistent with the cell expansion observed for **1red** to **1yellow** transition. Furthermore, the optimal volume of the *trans*-keto form of **1red** was calculated to be  $1036 \text{ \AA}^3$ , which is commensurate with the crystal structure of **1yellow**. The *trans*-keto form of **1red** was found to be considerably less stable than the enol or *cis*-keto (by  $\sim 22$  kcal mol<sup>-1</sup>) forms, as expected from the molecular calculations.

The energy difference between the enol and the *cis*-keto forms of **1yellow** (4.5 kcal mol<sup>-1</sup>) is largely accounted for by the 5.9 kcal mol<sup>-1</sup> difference in the energy between the enol and the *cis*-keto geometries as they lie in their optimized **1yellow** crystal structures. The preference of the *cis*-keto form in **1red**, on the other hand, relates more to the stronger intermolecular interactions in the *cis*-keto form of **1red** vs. the enol form. This difference between **1red** and **1yellow** is consistent with the fundamentally different nature of the intermolecular contacts, as shown in Fig. 2. The calculated interaction energy between molecules in the *cis*-keto form of **1red** is  $-55.3$  kcal mol<sup>-1</sup>, while the interaction energy between molecules in the enol form of **1red** is  $-50.8$  kcal mol<sup>-1</sup>.

In order to obtain some quantitative insight into the nature of intermolecular interactions we have performed the ETS-NOCV<sup>28</sup> analysis (ADF/BLYP-D3/TZP) based on the cluster models containing four monomers. It is established that the leading contribution to overall stabilization of both polymorphs is the dispersion one:  $\Delta E_{\text{dispersion}} = -87.38$  and  $-94.54$  kcal mol<sup>-1</sup> for **1red** and **1yellow**, respectively, followed by the electrostatic one:  $\Delta E_{\text{elstat}} = -48.06$  and  $-41.19$  kcal mol<sup>-1</sup> for **1red** and **1yellow**, respectively. The third contribution arises from the orbital interaction terms:  $\Delta E_{\text{orb}} = -36.34$  and  $-39.97$  kcal mol<sup>-1</sup> for **1red** and **1yellow**, respectively (Table S4 in the ESI†). In order to shed further light on the  $\Delta E_{\text{orb}}$  term we have plotted the overall deformation density ( $\Delta\rho_{\text{orb}}$ ) upon formation of tetramers of both polymorphs (Fig. S14 in the ESI†). It is seen that the formation of both tetramers leads to charge transfers within the following non-covalent interactions:  $\pi \cdots \pi$ , C-H $\cdots$  $\pi$ , C-H $\cdots$ O and C-H $\cdots$ H-C.

Finally, it is important to emphasize that the calculated band gaps in **1red** and **1yellow** systematically decrease in the following order: enol > *cis*-keto > *trans*-keto (Fig. S15 and S16 in the ESI†). For example, the band gaps are 1.90, 1.48 and 1.27 eV for the enol, *cis*-keto and *trans*-keto forms, respectively, of **1red** when constrained to the  $P2_1/c$  symmetry simulation cell that was determined from experiment. This trend relates well with the HOMO-LUMO gap of their

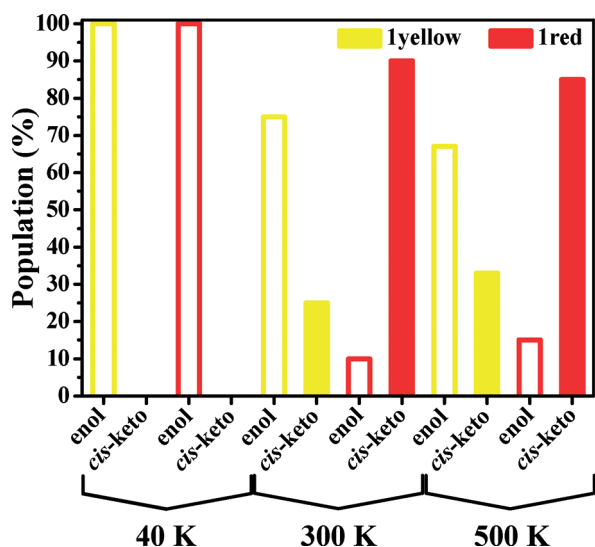


Fig. 12 Changes in population between enol and *cis*-keto forms in crystals of **1yellow** and **1red** at various temperatures. The blank and filled bars show the percentage of the enol and *cis*-keto forms, respectively, along the CP2K trajectory (100 ps). The two molecules were considered in the unit cell.

constituent molecules (Fig. 13) and explains the experimental data (Fig. 3 and 4).

## Conclusions

In summary, we have shown that *N,N'*-bis(3-methoxysalicylidene)-1,5-diiminonaphthalene can be prepared under two polymorphs distinguished by their colour, and their dihedral angle  $\Phi$  between the benzene and the naphthalene rings, from a structural viewpoint. X-ray powder diffraction reveals that **1red** irreversibly transforms above 165 °C into **1yellow** with a 3% increase of the molecular volume. Such expansion was also noticed from periodic DFT calculations.

Diffuse reflectance spectroscopy reveals a mixture of the dominant enol and *cis*-keto forms in the solid state at room temperature for **1red** and **1yellow**. Theoretical modelling based on static DFT periodic calculations and *ab initio* Born–Oppenheimer dynamics simulations of the crystals confirm that both polymorphs are indeed in the enol  $\leftrightarrow$  *cis*-keto equilibrium at room temperature (Fig. 12). However, the *cis*-keto population dominates for **1red**, whereas the enol is preferred in the case of **1yellow**. A higher population of the *cis*-keto form within **1red** might result in a higher population of the *trans*-keto isomer, which explains why **1red** turns to a darker red at high temperature, while **1yellow** changes to a brighter shade of red (Fig. 3). At low temperature solely the enol form is noted for both polymorphs (Fig. 12), which is consistent with the thermochromism to pale yellow on cooling. The calculated HOMO–LUMO band gaps correlate qualitatively with the experimental reflectance spectra.

Furthermore, **1red** clearly reveals features of the *trans*-keto form in the ground state as well as exhibits both thermochromic and photochromic properties. The latter property is observed upon irradiation at  $\lambda = 365$  nm. This photochromism exhibits slow back thermal relaxation ( $k = 6.0 \times 10^{-5} \text{ s}^{-1}$ ). **1yellow** exhibits thermochromism; however, no photochromism has been observed. Most interestingly, the *trans*-keto form can be populated on warming from **1yellow**,

which is observed for the first time for an anil molecule. The main emission properties of both polymorphs are originating from the *cis*-keto\* to *cis*-keto relaxation.

## Experimental

### Physical measurements

$^1\text{H}$  NMR spectra were obtained on a Bruker AC 300 MHz spectrometer at 25 °C. Diffuse reflectance spectra were obtained with a Varian Cary 5E spectrometer using polytetrafluoroethylene (PTFE) as a reference. Spectra were measured on pure solids to avoid matrix effects. Eventual distortions in the Kubelka–Munk spectra that could result from the study of pure compounds have not been considered because no comparison with absorption spectra was necessary. Solid-state emission spectra were obtained with a Fluorolog-3 (Jobin-Yvon-Spex Company) spectrometer. Kubelka–Munk and emission spectra were normalized to allow meaningful comparisons. Raman spectra in the solid state were obtained with a FTIR Nicolet Magna 860 spectrometer with Raman unit and Nd:YVO<sub>4</sub> ( $\lambda = 1064$  nm) laser. Light irradiations were carried out with a LOT-ORIEL 200 W high-pressure mercury arc lamp (LSN261). Simultaneous thermogravimetric (TG) and differential thermal (DTA) analyses were performed using an SDT 2960 Simultaneous DTA-TGA instrument in a dynamic air atmosphere (120 mL min<sup>-1</sup>) from room temperature to 900 °C with a 10 °C min<sup>-1</sup> heating rate. TG-MS analyses were performed on a Mettler TOLEDO TGA/SDTD851 spectrometer combined with a ThermoStar PFEIFFER VACUUM spectrometer in a dynamic air atmosphere (120 mL min<sup>-1</sup>) from room temperature to 900 °C with a 10 °C min<sup>-1</sup> heating rate. DSC measurements were carried out in a He(g) atmosphere using a Perkin–Elmer DSC Pyris 1 instrument working with hermetically sealed aluminum capsules. The heating and cooling rates were fixed at 10 K per minute. Thermal dependence of optical density was recorded on a Linkam temperature cell coupled with an Olympus BX51 optical microscope equipped with an ultrafast silicon photodiode over the temperature range from -190 to 200 °C with a 2 °C min<sup>-1</sup> rate. Topographic analysis of the crystal surface quality at ambient temperature was investigated by atomic force microscopy using an AFM NT-MDT Solver Pro-M model with a standard tip for semicontact mode. Elemental analyses were carried out on a CHNS HEKAtech EuroEA 3000 analyzer.

### Hirshfeld surface analysis

The Hirshfeld molecular surfaces<sup>13</sup> and their associated 2D fingerprint plots<sup>14</sup> were generated using the Crystal Explorer 3.1 software<sup>15</sup> on the basis of crystal structures. The  $d_{\text{norm}}$  (normalized contact distance) surface and the breakdown of the 2D fingerprint plots were used for decoding and quantifying the intermolecular interactions in the crystal lattice. The  $d_{\text{norm}}$  is a symmetric function of distances to the surface from the nuclei inside ( $d_i$ ) and outside ( $d_e$ ) the Hirshfeld surface, relative to their respective van der Waals radii. Negative values of  $d_{\text{norm}}$  indicating contacts shorter than the sum of

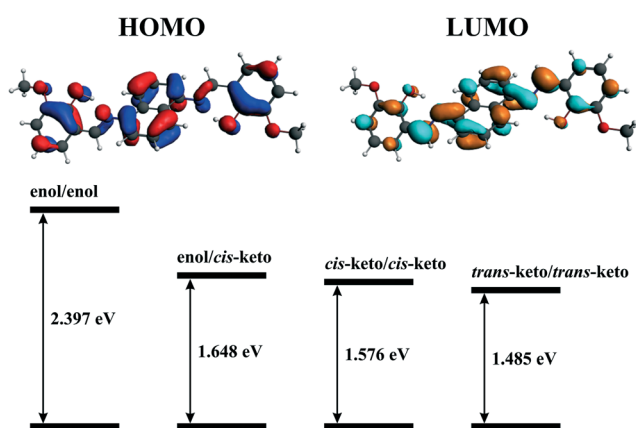


Fig. 13 The HOMO–LUMO gaps for single molecules of different isomers of **1**, obtained from ADF/DFT/BLYP-D3/TZP calculations. The contours of HOMO and LUMO orbitals (0.02 a.u.) are shown only for the enol isomer.

van der Waals radii are shown in red, while positive values of contacts longer than the sum of van der Waals radii are depicted in blue. The white colour is used for intermolecular distances close to van der Waals radii contacts with  $d_{\text{norm}}$  equal to zero. 2D fingerprint plots were generated using  $d_i$  and  $d_e$  in the translated 0.4–3.0 Å range and including reciprocal contacts as a pair of coordinates in 2D histograms. A colour gradient in the fingerprint plots ranging from blue to red is used to visualize the proportional contribution of contact pairs in the global surface.

### Enrichment ratio

The enrichment ratio ( $E$ )<sup>17</sup> of a pair of elements (X,Y) is the ratio between the proportion of actual contacts in the crystal and the theoretical proportion of random contacts.  $E$  is larger than unity for pairs of elements which have a high propensity to form contacts in crystals, while pairs which tend to avoid contacts with each other yield an  $E$  value lower than unity.  $E$  values are calculated from the percentage of contacts, which, in turn, are given by CrystalExplorer 3.1 software,<sup>15</sup> between one type or two types of chemical elements in a crystal packing.

### Density functional theory (DFT) based calculations

DFT based molecular and periodic calculations were performed based on the ADF<sup>25</sup> and VSAP<sup>26</sup> programs, respectively, with DFT/BLYP-D3/TZP.

### Dynamics simulations of crystals

DFT methods (CP2K package)<sup>27</sup> were applied in the Born–Oppenheimer approach of molecular dynamics. The 100 ps trajectory was obtained based on the BLYP functional with Grimme's dispersion corrections. The mixed DZVP basis sets and plane waves (cutoff = 260) were used. The time step was 1 fs. The trajectory was analyzed using the VMD program. Calculations were done based on a Nosé–Hover thermostat at 40, 300 and 500 K.

### ETS-NOCV bonding analysis

Natural orbitals for chemical valence (NOCV) are the eigenvectors that diagonalize the deformation density matrix.<sup>28</sup> It was shown that the natural orbitals for chemical valence pairs ( $\psi_{-k}$ ,  $\psi_k$ ) decompose the differential density  $\Delta\rho$  into NOCV contributions ( $\Delta\rho_k$ ):

$$\Delta\rho(r) = \sum_{k=1}^{M/2} v_k [-\psi_{-k}^2(r) + \psi_k^2(r)] = \sum_{k=1}^{M/2} \Delta\rho_k(r)$$

where  $v_k$  and  $M$  stand for the NOCV eigenvalues and the number of basis functions, respectively. Visual inspection of deformation density plots ( $\Delta\rho_k$ ) helps to attribute the symmetry and direction of the charge flow. In addition, these pictures are enriched by providing the energetic estimations,  $\Delta E_{\text{orb}}(k)$ , for each  $\Delta\rho_k$  within the ETS-NOCV scheme.<sup>29</sup> The exact formula, which links the ETS and NOCV methods, will be

given in the next paragraph, after we briefly present the basic concept of the ETS scheme. In this method the total bonding energy  $\Delta E_{\text{total}}$  between interacting fragments, exhibiting geometry as in the combined complex, is divided into the three components:  $\Delta E_{\text{total}} = \Delta E_{\text{elstat}} + \Delta E_{\text{Pauli}} + \Delta E_{\text{orb}}$ . The first term,  $\Delta E_{\text{elstat}}$ , corresponds to the classical electrostatic interaction between the promoted fragments as they are brought to their positions in the final complex. The second term,  $\Delta E_{\text{Pauli}}$ , accounts for the repulsive Pauli interaction between occupied orbitals on the two fragments in the combined molecule. Finally, the last stabilizing term,  $\Delta E_{\text{orb}}$ , represents interactions between the occupied molecular orbitals of one fragment with the unoccupied molecular orbitals of the other fragment as well as mixing of occupied and virtual orbitals within the same fragment (inner-fragment polarization). This energy term may be linked to the electronic bonding effect coming from the formation of a chemical bond. In the combined ETS-NOCV scheme<sup>27</sup> the orbital interaction term,  $\Delta E_{\text{orb}}$ , is expressed in terms of NOCV's eigenvalues ( $v_k$ ) as:

$$\Delta E_{\text{orb}} = \sum_k \Delta E_{\text{orb}}(k) = \sum_{k=1}^{M/2} v_k [-F_{-k,-k}^{\text{TS}} + F_{k,k}^{\text{TS}}]$$

where  $F_{i,i}^{\text{TS}}$  are diagonal Kohn–Sham matrix elements defined over NOCV with respect to the transition state (TS) density at the midpoint between the density of the molecule and the sum of fragment densities. The above components  $\Delta E_{\text{orb}}(k)$  provide the energetic estimation of  $\Delta\rho_k$  that may be related to the importance of a particular electron flow channel for the bonding between the considered molecular fragments. ETS-NOCV analysis was done based on the Amsterdam Density Functional (ADF) package<sup>25</sup> in which this scheme was implemented. We have applied BLYP-D3/TZP computational details as it has been shown that they provide accurate results on non-covalent interactions.

### Synthesis of 1red and 1yellow

A solution of *o*-vanilin (10 mmol, 1.522 g) dissolved in ethanol (20 mL) was added to a solution of 1,5-diaminonaphthalene (5 mmol, 0.791 g) in ethanol (20 mL). The mixture was stirred for 30 min and, afterwards, heated at reflux for 2 h. The resulting red solution was allowed to cool to room temperature to give crystals of **1red**. Recrystallization of **1red** from acetone gives crystals of **1yellow**. Recrystallization of **1yellow** from ethanol or methanol gives crystals of **1red**. <sup>1</sup>H NMR spectra of both **1red** and **1yellow** are the same regardless of the solvent. <sup>1</sup>H NMR (CDCl<sub>3</sub>):  $\delta$  = 3.99 (s, 6H, CH<sub>3</sub>), 6.97 (t, <sup>3</sup>J<sub>H,H</sub> = 7.8 Hz, 2H, *m*-H, C<sub>6</sub>H<sub>3</sub>), 7.08 (d, <sup>3</sup>J<sub>H,H</sub> = 7.8 Hz, 2H, *o*-H, C<sub>6</sub>H<sub>3</sub>), 7.13 (d, <sup>3</sup>J<sub>H,H</sub> = 7.8 Hz, 2H, *p*-H, C<sub>6</sub>H<sub>3</sub>), 7.32 (d, <sup>3</sup>J<sub>H,H</sub> = 7.7 Hz, 2H, *p*-H, C<sub>10</sub>H<sub>6</sub>), 7.58 (t, <sup>3</sup>J<sub>H,H</sub> = 7.8 Hz, 2H, *m*-H, C<sub>10</sub>H<sub>6</sub>), 8.28 (d, <sup>3</sup>J<sub>H,H</sub> = 7.8 Hz, 2H, *o*-H, C<sub>10</sub>H<sub>6</sub>), 8.78 (s, 2H, CHN), 13.88 (s, 2H, OH) ppm. <sup>1</sup>H NMR (DMSO-*d*<sub>6</sub>):  $\delta$  = 3.87 (s, 6H, CH<sub>3</sub>), 6.97 (t, <sup>3</sup>J<sub>H,H</sub> = 8.0 Hz, 2H, *m*-H, C<sub>6</sub>H<sub>3</sub>), 7.21 (t, <sup>3</sup>J<sub>H,H</sub> = 8.0 Hz, 2H, *m*-H, C<sub>6</sub>H<sub>3</sub>), 7.37 (d, <sup>3</sup>J<sub>H,H</sub> = 8.0 Hz, 2H, *p*-H, C<sub>6</sub>H<sub>3</sub>), 7.53 (d, <sup>3</sup>J<sub>H,H</sub> = 7.8 Hz, 2H, *p*-H, C<sub>10</sub>H<sub>6</sub>), 7.69 (t, <sup>3</sup>J<sub>H,H</sub> = 7.8 Hz, 2H, *m*-H, C<sub>10</sub>H<sub>6</sub>), 8.14

(d,  $^3J_{\text{H,H}} = 7.8$  Hz, 2H, *o*-H, C<sub>10</sub>H<sub>6</sub>), 9.06 (s, 2H, CHN), 13.09 (s, 2H, OH) ppm. Calc. for C<sub>26</sub>H<sub>22</sub>N<sub>2</sub>O<sub>4</sub> (426.47): C 73.23, H 5.20; N 6.57. Found: C 73.29, H 5.16, N 6.59.

### Single-crystal X-ray diffraction study

X-ray data collection was performed on a Mar345 image plate detector using Mo-K $\alpha$  radiation (Zr-filter) at ambient temperature. The data were integrated with the crysAlisPro software.<sup>30</sup> The implemented empirical absorption correction was applied. The structures were solved by direct methods using the SHELXS-97 program<sup>31</sup> and refined by full-matrix least squares on  $|F^2|$  using SHELXL-97.<sup>31</sup> Non-hydrogen atoms were anisotropically refined and the hydrogen atoms were placed on calculated positions in riding mode with temperature factors fixed at 1.2 times  $U_{\text{eq}}$  of the parent atoms and 1.5 times  $U_{\text{eq}}$  for methyl groups. Figures were generated using the program Mercury.<sup>32</sup>

**Crystal data for 1red.** C<sub>26</sub>H<sub>22</sub>N<sub>2</sub>O<sub>4</sub>,  $M_r = 426.46$  g mol<sup>-1</sup>, monoclinic, space group  $P2_1/c$ ,  $a = 14.0292(9)$ ,  $b = 5.0669(4)$ ,  $c = 14.7229(11)$  Å,  $\beta = 99.433(7)^\circ$ ,  $V = 1032.42(13)$  Å<sup>3</sup>,  $Z = 2$ ,  $\rho = 1.372$  g cm<sup>-3</sup>,  $\mu(\text{Mo-K}\alpha) = 1.372$  mm<sup>-1</sup>, reflections: 2931 collected, 2931 unique,  $R_{\text{int}} = 0.000$ ,  $R_1(\text{all}) = 0.0620$ ,  $wR_2(\text{all}) = 0.1476$ .

**Crystal data for 1yellow.** C<sub>26</sub>H<sub>22</sub>N<sub>2</sub>O<sub>4</sub>,  $M_r = 426.46$  g mol<sup>-1</sup>, monoclinic, space group  $P2_1/n$ ,  $a = 6.7362(6)$ ,  $b = 24.2039(15)$ ,  $c = 6.8686(5)$  Å,  $\beta = 112.293(9)^\circ$ ,  $V = 1036.17(15)$  Å<sup>3</sup>,  $Z = 2$ ,  $\rho = 1.367$  g cm<sup>-3</sup>,  $\mu(\text{Mo-K}\alpha) = 0.093$  mm<sup>-1</sup>, reflections: 7641 collected, 1954 unique,  $R_{\text{int}} = 0.055$ ,  $R_1(\text{all}) = 0.0519$ ,  $wR_2(\text{all}) = 0.1073$ .

### Powder X-ray diffraction study

*In situ* powder diffraction was performed using a MAR345 image plate diffractometer and MoK $\alpha$  radiation from a Rigaku UltraX-18 rotating anode generator. An Oxford Cryostream 700 cooler and a Leister Le Mini Sensor Kit were used to cool and heat the samples. The latter were filled in 0.5 mm glass capillaries placed 200 mm from the detector. The capillaries with sample were cooled/heated at a rate of 27 to 30 °C per hour, while X-ray powder diffraction data were collected. Each pattern was collected during 3 minutes of exposure, while the capillary was rotated by 60 degrees. **1red** and **1yellow** were characterized at temperatures from -183 to 127 °C, both on cooling and heating, and on heating from room temperature to 300 °C. The data were integrated using the Fit2D program<sup>33</sup> and a calibration measurement of a NIST LaB<sub>6</sub> standard sample. Uncertainties of the integrated intensities were calculated at each  $2\theta$ -point by applying Poisson statistics to the intensity data, considering the geometry of the detector, similar to a recently described procedure.<sup>34</sup> The calculated absorption coefficient is practically equal to zero, thus the absorption correction was not applied. The temperature dependence of the cell and other structural parameters was obtained *via* a sequential Rietveld refinement implemented into Fullprof.<sup>35</sup> The background was described by linear interpolation between selected points.

## Acknowledgements

This work was funded by the Fonds National de la Recherche Scientifique (FNRS) (PDR T.0102.15), Romanian National Authority for Scientific Research, CNCS – UEFISCDI, project number PN-II-RU-TE-2014-4-2695, Contract Number 267/01.10.2015, WBI and Academie Roumaine. We also thank the F.R.S.-FNRS (Belgium) and WBI for post-doctoral positions allocated to D. A. S. and M. G. B. DFT calculations were performed using PL-Grid Infrastructure and resources provided by ACC Cyfronet AGH (Cracow, Poland) we thank the COST action MP1202. Mr. A. Railliet is thanked for his help with calorimetric measurements.

## References

- 1 C. Bertarellia, A. Biancoc, R. Castagnaa and G. Pariania, *J. Photochem. Photobiol., C*, 2011, **12**, 106 and references therein.
- 2 P. Bamfield and M. G. Hutchings, *Chromic Phenomena; technological applications of colour chemistry*, Royal Society of Chemistry, Cambridge, 2010.
- 3 (a) M. Irie, *Chem. Rev.*, 2000, **100**, 1683; (b) S. Kobatake and M. Irie, *Annu. Rep. Prog. Chem., Sect. C: Phys. Chem.*, 2003, **99**, 277.
- 4 (a) E. Hadjoudis, M. Vitterakis, I. Moustakali and I. Mavridis, *Tetrahedron*, 1987, **43**, 1345; (b) E. Hadjoudis and I. M. Mavridis, *Chem. Soc. Rev.*, 2004, **33**, 579; (c) K. Amimoto and T. Kawato, *J. Photochem. Photobiol., C*, 2005, **6**, 207; (d) T. Haneda, M. Kawano, T. Kojima and M. Fujita, *Angew. Chem., Int. Ed.*, 2007, **46**, 6643; (e) E. Hadjoudis, S. D. Chatziefthimiou and I. M. Mavridis, *Curr. Org. Chem.*, 2009, **13**, 269; (f) Y. Inokuma, M. Kawano and M. Fujita, *Nat. Chem.*, 2011, **3**, 349.
- 5 E. Hadjoudis, V. Verganelakis, C. Trapalis and G. Kordas, *Mol. Eng.*, 2000, **8**, 459.
- 6 P.-L. Jacquemin, Y. Garcia and M. Devillers, *J. Mater. Chem. C*, 2014, **2**, 1815.
- 7 (a) F. Robert, A. D. Naik, B. Tinant, R. Robiette and Y. Garcia, *Chem. – Eur. J.*, 2009, **15**, 4327; (b) F. Robert, A. D. Naik, B. Tinant and Y. Garcia, *Inorg. Chim. Acta*, 2012, **380**, 104; (c) Y. Garcia, F. Robert, A. D. Naik, G. Zhou, B. Tinant, K. Robeyns, S. Michotte and L. Piraux, *J. Am. Chem. Soc.*, 2011, **133**, 15850; (d) F. Robert, A. D. Naik and Y. Garcia, *J. Phys.: Conf. Ser.*, 2010, **217**, 012031.
- 8 (a) F. Robert, A. D. Naik, F. Hidara, B. Tinant, R. Robiette, J. Wouters and Y. Garcia, *Eur. J. Org. Chem.*, 2010, 621; (b) F. Robert, P.-L. Jacquemin, B. Tinant and Y. Garcia, *CrystEngComm*, 2012, **14**, 4396; (c) D. A. Safin, K. Robeyns and Y. Garcia, *CrystEngComm*, 2012, **14**, 5523; (d) D. A. Safin, K. Robeyns and Y. Garcia, *RSC Adv.*, 2012, **2**, 11379.
- 9 (a) P.-L. Jacquemin, K. Robeyns, M. Devillers and Y. Garcia, *Chem. Commun.*, 2014, **50**, 649; (b) P.-L. Jacquemin, K. Robeyns, M. Devillers and Y. Garcia, *Chem. – Eur. J.*, 2015, **21**, 6832.
- 10 (a) M. S. M. Rawat and J. L. Norula, *Indian J. Chem., Sect. B: Org. Chem. Incl. Med. Chem.*, 1987, **26**, 232; (b) Y. Yildiz, Z. Kiliç and T. Hökelek, *J. Mol. Struct.*, 1988, **441**, 1; (c) N. Hoshino, T. Inabe, T. Mitani and Y. Maruyama, *Bull. Chem.*

- Soc. Jpn.*, 1988, **61**, 4207; (d) T. Inabe, N. Hoshino, T. Mitani and Y. Maruyama, *Bull. Chem. Soc. Jpn.*, 1989, **62**, 2245; (e) E. Ito, H. Oji, T. Araki, K. Oichi, H. Ishii, Y. Ouchi, T. Ohta, N. Kosugi, Y. Maruyama, T. Naito, T. Inabe and K. Seki, *J. Am. Chem. Soc.*, 1997, **119**, 6336; (f) T. Sekikawa, T. Kobayashi and T. Inabe, *J. Phys. Chem. B*, 1997, **1**, 10645; (g) Z. Popović, V. Roje, G. Pavlović, D. Matković-Calogović and G. Giester, *J. Mol. Struct.*, 2001, **597**, 39; (h) E. Hadjoudis, A. Rontoyianni, K. Ambroziak, T. Dziembowska and I. Mavridis, *J. Photochem. Photobiol. A*, 2004, **162**, 521; (i) M. Taneda, K. Amimoto, H. Koyama and T. Kawato, *Org. Biomol. Chem.*, 2004, **1**, 499; (j) T. Fujiwara, J. Hadara and O. Keiichiro, *J. Phys. Chem. B*, 2004, **108**, 4035; (k) M. Ziólek, J. Kubicki, A. Maciejewski, R. Naskręcki and A. Grabowska, *J. Chem. Phys.*, 2006, **124**, 124518; (l) P. Xue, R. Lu, G. Chen, Y. Zhang, H. Nomoto, M. Takafuji and H. Ihara, *Chem. – Eur. J.*, 2007, **13**, 8231; (m) M. Ziólek, G. Burzinski and J. Karolczak, *J. Phys. Chem. A*, 2009, **113**, 2854; (n) P. Chen, R. Lu, P. Xue, T. Xu, G. Chen and Y. Zhao, *Langmuir*, 2009, **25**, 8395; (o) M. Taneda, H. Koyama and T. Kawato, *Chem. Lett.*, 2007, **36**, 354; (p) M. Taneda, H. Koyama and T. Kawato, *Res. Chem. Intermed.*, 2009, **35**, 643.
- 11 (a) K. Tanaka, R. Shimoura and M. R. Caira, *Tetrahedron Lett.*, 2010, **51**, 449; (b) D. A. Safin and Y. Garcia, *RSC Adv.*, 2013, **3**, 6466.
- 12 G. Ceyhan, M. Köse, V. McKee, S. Uruş, A. Gölcü and M. Tümer, *Spectrochim. Acta, Part A*, 2012, **95**, 382.
- 13 M. A. Spackman and D. Jayatilaka, *CrystEngComm*, 2009, **11**, 19.
- 14 M. A. Spackman and J. J. McKinnon, *CrystEngComm*, 2002, **4**, 378.
- 15 S. K. Wolff, D. J. Grimwood, J. J. McKinnon, M. J. Turner, D. Jayatilaka and M. A. Spackman, *CrystalExplorer 3.1*, University of Western Australia, 2012.
- 16 (a) D. A. Safin, M. P. Mitoraj, K. Robeyns, Y. Filinchuk and C. M. L. Vande Velde, *Dalton Trans.*, 2015, **44**, 16824; (b) M. G. Babashkina, K. Robeyns, Y. Filinchuk and D. A. Safin, *New J. Chem.*, 2016, **40**, 1230.
- 17 C. Jelsch, K. Ejsmont and L. Huder, *IUCrJ*, 2014, **1**, 119.
- 18 T. Fujiwara, J. Hadara and O. Keiichiro, *J. Phys. Chem. B*, 2004, **108**, 4035.
- 19 D. A. Safin, M. Bolte and Y. Garcia, *CrystEngComm*, 2014, **16**, 5524.
- 20 M. Sliwa, S. Létard, I. Malfant, M. Nierlich, P. G. Lacroix, T. Asahi, H. Masuhara, P. Yu and K. Nakatani, *Chem. Mater.*, 2005, **17**, 4727.
- 21 T. Kawato, H. Koyama, H. Kanatomi and M. Isshiki, *J. Photochem.*, 1985, **28**, 103.
- 22 T. Kawato, H. Kanatomi, H. Koyama and T. Igarashi, *J. Photochem.*, 1986, **33**, 199.
- 23 J. Harada, T. Fujiwara and K. Ogawa, *J. Am. Chem. Soc.*, 2007, **129**, 16216.
- 24 For example: (a) R. Ababei, C. Pichon, O. Roubeau, Y.-G. Li, N. Brefuel, L. Buisson, P. Guionneau, C. Mathonière and R. Clérac, *J. Am. Chem. Soc.*, 2013, **135**, 14840; (b) C. Mathoniere, H.-J. Lin, D. Siretanu, R. Clérac and J. M. Smith, *J. Am. Chem. Soc.*, 2013, **135**, 19083; (c) C. Lefter, S. Tricard, P. Simon, H. Peng, G. Molnar, L. Salmon, P. Demont, A. Rotaru and A. Bousseksou, *J. Phys. Chem. C*, 2015, **119**, 8522; (d) T. Zhao, L. Cuignet, M. M. Dirtu, M. Wolff, V. Spasojevic, I. Boldog, A. Rotaru, Y. Garcia and C. Janiak, *J. Mater. Chem. C*, 2015, **3**, 7802.
- 25 ADF 2012.01: (a) G. te Velde, F. M. Bickelhaupt, E. J. Baerends, C. Fonseca Guerra, S. J. A. van Gisbergen, J. G. Snijders and T. Ziegler, *J. Comput. Chem.*, 2001, **22**, 931 and references therein; (b) E. J. Baerends, J. Autschbach, D. Bashford, A. Bérces, F. M. Bickelhaupt, C. Bo, P. M. Boerrigter, L. Cavallo, D. P. Chong, L. Deng, R. M. Dickson, D. E. Ellis, M. van Faassen, L. Fan, T. H. Fischer, C. Fonseca Guerra, A. Ghysels, A. Giammona, S. J. A. van Gisbergen, A. W. Götz, J. A. Groeneveld, O. V. Gritsenko, M. Grüning, F. E. Harris, P. van den Hoek, C. R. Jacob, H. Jacobsen, L. Jensen, G. van Kessel, F. Kootstra, M. V. Krykunov, E. van Lenthe, D. A. McCormack, A. Michalak, M. Mitoraj, J. Neugebauer, V. P. Nicu, L. Noodleman, V. P. Osinga, S. Patchkovskii, P. H. T. Philipsen, D. Post, C. C. Pye, W. Ravenek, J. I. Rodriguez, P. Ros, P. R. T. Schipper, G. Schreckenbach, M. Seth, J. G. Snijders, M. Solà, M. Swart, D. Swerhone, G. te Velde, P. Vernooijs, L. Versluis, L. Visscher, O. Visser, F. Wang, T. A. Wesolowski, E. M. van Wezenbeek, G. Wiesenekker, S. K. Wolff, T. K. Woo, A. L. Yakovlev and T. Ziegler, *Theoretical Chemistry*, Vrije Universiteit, Amsterdam.
- 26 (a) G. Kresse and J. Hafner, *Phys. Rev. B: Condens. Matter Mater. Phys.*, 1993, **47**, 558; (b) G. Kresse and J. Furthmüller, *Phys. Rev. B: Condens. Matter Mater. Phys.*, 1996, **54**, 11169.
- 27 (a) J. Vande Vondele and J. Hutter, *J. Chem. Phys.*, 2003, **118**, 4365; (b) M. Krack and M. Parrinello, *Forschungszentrum Jülich, NIC Series*, 2004, vol. 25, p. 29; (c) J. Vande Vondele, M. Krack, F. Mohamed, M. Parrinello, T. Chassaing and J. Hutter, *Comput. Phys. Commun.*, 2005, **167**, 103.
- 28 (a) M. Mitoraj and A. Michalak, *J. Mol. Model.*, 2007, **13**, 347; (b) A. Michalak, M. Mitoraj and T. Ziegler, *J. Phys. Chem. A*, 2008, **112**, 1933; (c) M. Mitoraj, A. Michalak and T. Ziegler, *J. Chem. Theory Comput.*, 2009, **5**, 962.
- 29 (a) W. Gao, H. Feng, X. Xuan and L. Chen, *J. Mol. Model.*, 2012, **18**, 4577; (b) T. van der Wijst, C. Fonseca Guerra, M. Swart, F. M. Bickelhaupt and B. Lippert, *Angew. Chem., Int. Ed.*, 2009, **48**, 3285; (c) L. P. Wolters, N. W. G. Smits and C. F. Guerra, *Phys. Chem. Chem. Phys.*, 2015, **17**, 1585.
- 30 *Oxford Diffraction Data collection and data reduction, Version 171.34.40*.
- 31 G. M. Sheldrick, *Acta Crystallogr., Sect. A: Found. Crystallogr.*, 2008, **64**, 112.
- 32 I. J. Bruno, J. C. Cole, P. R. Edgington, M. Kessler, C. F. Macrae, P. McCabe, J. Pearson and R. Taylor, *Acta Crystallogr., Sect. B: Struct. Sci.*, 2002, **58**, 389.
- 33 A. P. Hammersley, S. O. Svensson, M. Hanfland, A. N. Fitch and D. Häusermann, *High Pressure Res.*, 1996, **14**, 235.
- 34 S. Vogel, L. Ehm, K. Knorr and G. Braun, *Adv. X-Ray Anal.*, 2002, **45**, 31.
- 35 J. Rodriguez-Carvajal, *Phys. B*, 1993, **192**, 55.